Properties of eigenmodes and quantum-chaotic scattering in a superconducting microwave Dirac billiard with threefold rotational symmetry

Weihua Zhang [1,2,*], Xiaodong Zhang [1], Jiongning Che [1], Maksym Miski-Oglu, [3] and Barbara Dietz [1,2,†]

[1] *Lanzhou Center for Theoretical Physics and the Gansu Provincial Key Laboratory of Theoretical Physics, Lanzhou University, Lanzhou, Gansu 730000, China*

[2] *Center for Theoretical Physics of Complex Systems, Institute for Basic Science (IBS), Daejeon 34126, Korea*

[3] *GSI Helmholtzzentrum für Schwerionenforschung GmbH, D-64291 Darmstadt, Germany*

(Received 16 February 2023; revised 16 April 2023; accepted 18 April 2023; published 27 April 2023)

We report on experimental studies that were performed with a microwave Dirac billiard (DB), that is, a flat resonator containing metallic cylinders arranged on a triangular grid, whose shape has a threefold rotational (C_3) symmetry. Its band structure exhibits two Dirac points (DPs) that are separated by a nearly flat band. We present a procedure that we employed to identify eigenfrequencies and to separate the eigenstates according to their transformation properties under rotation by $\frac{2\pi}{3}$ into the three C_3 subspaces. This allows us to verify previous numerical results of Zhang and Dietz [Phys. Rev. B **104**, 064310 (2021)], thus confirming that the properties of the eigenmodes coincide with those of artificial graphene around the lower DP, and they are well described by a tight-binding model for a honeycomb-kagome lattice of corresponding shape. Above all, we investigate the properties of the wave-function components in terms of the fluctuation properties of the measured scattering matrix, which are numerically not accessible. They are compared to random-matrix theory predictions for quantum-chaotic scattering systems exhibiting extended or localized states in the interaction region, that is, the DB. Even in regions where the wave functions are localized, the spectral properties coincide with those of typical quantum systems with chaotic classical counterparts.

DOI: 10.1103/PhysRevB.107.144308

I. INTRODUCTION

Superconducting microwave Dirac billiards (DBs) have been used for more than a decade to investigate fluctuation properties in the energy spectra of artificial graphene and fullerene structures [1–9]. The experiments presented in this work were performed with the DB shown schematically in Fig. 1, whose shape has a C_3 symmetry. The frequency was restricted to the range of the lowest transverse-magnetic (TM) mode, where the electric-field strength is perpendicular to the resonator plane and thus is governed by the scalar Helmholtz equation with Dirichlet boundary conditions (BCs) at the sidewalls of the cavity and cylinders. The Helmholtz equation is mathematically identical to the Schrödinger equation of a quantum billiard (QB) of corresponding shape, into which scatterers are inserted at the positions of the cylinders. The crucial advantage of such resonators as compared to honeycomb structures constructed from dielectric disks [10] is that superconducting high-precision measurements can be performed, which is indispensable for the determination of complete sequences of resonance frequencies.

The band structure of propagating modes of the DB exhibits two Dirac points (DPs), where the first and second and the fourth and fifth band, respectively, touch each other conically, and a nearly flat third band (FB) in between. This is reminiscent of a honeycomb-kagome billiard (HKB) whose sites form a combination of a honeycomb and a kagome sublattice [11–16]; see the uppermost inset of Fig. 1. Indeed, below the FB the electric-field intensities are maximal at the voids, which are located at the centers of three neighboring metallic cylinders (gray disks), marked with red and turquoise dots in Fig. 1, and they form a honeycomb structure. In the frequency range of the FB, they are maximal at the centers between adjacent cylinders, marked by black dots, that are at the sites of a kagome lattice, and above the FB on all sites of the HKB [15,16]. We demonstrated that below the FB the properties of DBs are well captured by a tight-binding model (TBM) for a graphene billiard (GB) [1,7,8], and generally by one for a HKB [15,16]. Dirac points are a characteristic of graphene that attracted a lot of attention [17–19] because in the region of the conical valleys graphene features relativistic phenomena [17–27], which triggered numerous realizations [28] of artificial graphene [2,10,29–43]. In the vicinity of the band edges (BEs), the spectral properties coincide with those of a nonrelativistic QB of corresponding shape [1,4,8].

The classical dynamics of a billiard with the shape of the DB shown in Fig. 1 is chaotic [16,44]. According to the Bohigas-Giannoni-Schmit conjecture, the fluctuation properties in the energy spectra of nonrelativistic quantum systems with a chaotic classical counterpart are universal [45–48] and coincide with those of random matrices from the Gaussian orthogonal ensemble (GOE) for time-reversal ($\mathcal{T}$) invariant systems and the Gaussian unitary ensemble (GUE) if $\mathcal{T}$ invariance is violated. Yet there also exist billiards with

*zhangwh2018@gmail.com

†Corresponding author: bdietzp@gmail.com

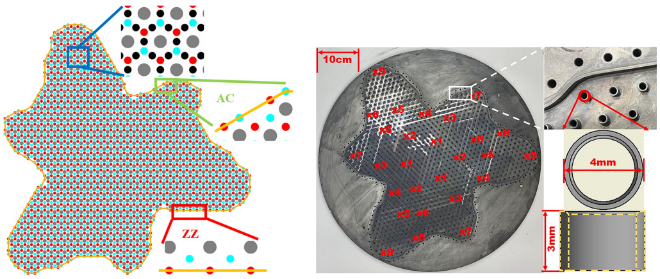

FIG. 1. Left panel: Schematic view of the Dirac billiard, which comprises 1033 metallic cylinders (gray disks) arranged on a triangular grid. In the uppermost inset, red and turquoise dots indicate the positions of the voids. They are located on the interpenetrating triangular sublattices of the honeycomb lattice, which is terminated by zigzag (ZZ) and armchair (AC) edges, as indicated in the lower insets. The centers between two neighboring cylinders, marked by black dots, form a kagome structure. Right panel: Photograph of the basin of the resonator. The metallic cylinders are milled out of a circular brass plate with radius $R = 570$ mm and height 19.5 mm. The red numbers denote the nine groups of, respectively, three antennas. To achieve superconductivity, the basin and the lid, which is a circular brass plate of radius R and height 6 mm with screw holes at the positions of the cylinders and along the boundary, are covered with a lead coating, whose critical temperature is $T_c = 7.2$ K, and then tightly screwed together through all holes. The resonator was cooled down to 4–6 K in a cryogenic chamber constructed by ULVAC Cryogenics in Kyoto, Japan. The inset to the right shows a zoom into one of the cylinders of diameter 4 mm and height 3 mm. The upper part is designed with a cut edge shape, as indicated by the yellow dashed lines, to achieve good electrical contact with the lid [1].

certain shapes that do not comply with this conjecture. Examples are billiards whose shape has C_3 symmetry [44,49,50], a unidirectional classical dynamics [51–54], or nanoelectromechanical systems consisting of a circular quantum dot on a suspended nanoscopic dielectric plate [55,56]. Their spectral properties may coincide with those of generic chaotic systems with violated time-reversal invariance even though it is preserved. The boundary of the DB has a C_3 symmetry. We actually chose the same shape as in the experiments that were performed 20 years ago with a superconducting microwave billiard in the range below the cutoff frequency f^{cut} of the first transverse-electric mode to investigate the spectral properties of the corresponding quantum billiard [44,50]. Interest in this QB arose due to theoretical predictions [49,57–59] that the spectral properties of part of the spectrum coincide with those of random matrices from the GUE. The origin of these discrepancies is outlined in Sec. II.

The objective of [16] and the present work was the numerical and experimental study of the properties of DBs and corresponding GBs and HKBs, whose boundary has a C_3 symmetry, especially in the relativistic region around the DPs. In the region of the conical valleys, which are located on, respectively, three of the corners of the first Brillouin zone [60], the two sets of valley eigenstates are well described by Dirac Hamiltonians for massless spin-1/2 quasiparticles [18,19]. Therefore, we also investigated in Ref. [16] properties of relativistic neutrino billiards (NBs) of corresponding shape. They were introduced in Ref. [61], and they are governed by the Weyl equation [62] for a spin-1/2 particle. The associated Dirac Hamiltonian is not invariant under time reversal, so the spectral properties of NBs with the shape of a chaotic billiard typically coincide with those of random matrices from the GUE if the shape has no geometric symmetries. It has been demonstrated in Refs. [63,64] that the spectral properties of GBs and NBs of corresponding shape do not coincide [1,8,24,28,65–71]. These discrepancies were attributed to intervalley scattering at the boundary of GBs [67,70,71]. Similar observations were made for HKBs [15,16].

In this work, we present experimental results for the DB shown in Fig. 1. In Sec. II we briefly review the properties of the billiard systems that were investigated in [16] and the results. Then, in Sec. III we provide information on the DB and experiment. Properties of the eigenmodes [16] are analyzed in Sec. IV and compared to those of the corresponding GB, QB, and NB. We also analyzed fluctuation properties of the scattering (S) matrix describing the measurement process [72]. Furthermore, we investigated strength distributions [73,74], which give information on the product of wave-function components at the positions of the antennas, and thus on their intensity distribution, and we demonstrate that they provide a tool to detect localization, i.e., scarred wave functions, as outlined in Sec. V. Finally, in Sec. VI we discuss and evaluate the results.

II. REVIEW OF THE THEORETICAL AND NUMERICAL RESULTS

The domain Ω of the DB shown in Fig. 1 is defined in the complex plane $w(r,\phi) = x(r,\phi) + iy(r,\phi)$ with $\phi \in [0, 2\pi)$, $r = [0, r_0]$ by the parametrization

$$w(r,\phi) = r[1 + 0.2\cos(3\phi) - 0.2\sin(6\phi)]e^{i\phi}. \tag{1}$$

The boundary $\partial\Omega$ is given by $w(r = r_0, \phi)$. The eigenfunctions $\psi(r,\phi)$ of the QB with this shape and the electric-field strength of the corresponding microwave billiard below f^{cut} [75–77] are governed by the Schrödinger equation with Dirichlet BCs along $\partial\Omega$. The solutions can be separated into the three irreducible subspaces associated with the C_3 symmetry, which are defined by the transformation properties of the eigenfunctions under rotation by $\frac{2l\pi}{3}$, $l = 0, 1, 2$. The rotation operator is given by

$$\hat{R} = e^{i\frac{2\pi}{3}\hat{L}}, \tag{2}$$

with $\hat{L}$ denoting the angular momentum operator. Applying it to the eigenfunctions of the QB yields for the symmetry-projected ones

$$\hat{R}^{\lambda}\psi_m^{(l)}(r,\phi) = \psi_m^{(l)}\left(r, \phi - \frac{2\pi}{3}\lambda\right) = e^{i\frac{2l\pi}{3}\lambda}\psi_m^{(l)}(r,\phi), \tag{3}$$

where

$$[\hat{R}, \hat{H}] = 0. \tag{4}$$

For $l = 0$, the wave functions are real and rotationally invariant, and thus invariant under the time-reversal operator $\hat{T} = \hat{\mathcal{C}}$, with $\hat{\mathcal{C}}$ denoting the complex conjugation operator [78]. In

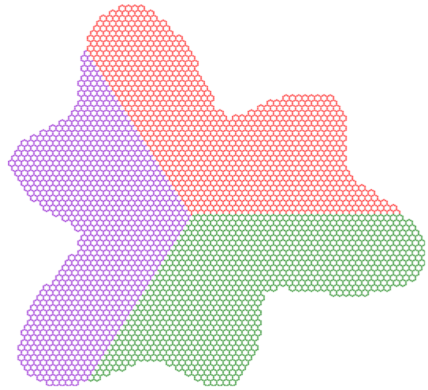

FIG. 2. Illustration of the procedure used to construct the GB and HKB. They are obtained by rotating a wegde with the shape of a fundamental domain, e.g., the red one, twice around its tip yielding the purple and green ones.

contrast, for $l = 1, 2$ they are complex and

$$\hat{T}\psi_m^{(1,2)}(r,\phi) = \psi_m^{(2,1)}(r,\phi), \tag{5}$$

implying that $\psi_m^{(1)}(r,\phi)$ and $\psi_m^{(2)}(r,\phi)$ are eigenfunctions with the same eigenvalue k_m^2. Thus, the eigenvalue spectrum can be separated into nondegenerate eigenvalues (singlets) and pairwise degenerate ones (doublets). If the corresponding classical dynamics is chaotic and if the billiard boundary has no additional symmetries, the spectral properties of the singlets show GOE behavior, while those of the two doublet partners exhibit GUE statistics [49].

Similarly, the eigenstates of GBs and HKBs with C_3 symmetry can be classified according to their transformation properties under rotation by $\frac{2\pi}{3}$. The matrix elements of the associated TBM Hamiltonian are given by

$$\hat{\mathcal{H}}_{ij}^{\mathrm{TBM}} = t_0\delta_{ij} + t_1\hat{\delta}(|\boldsymbol{r}_i - \boldsymbol{r}_j| - d_0) + t_2\hat{\delta}(|\boldsymbol{r}_i - \boldsymbol{r}_j| - d_1),$$

where $\hat{\delta}(x)$ equals unity for $x = 0$ and is zero otherwise, $\boldsymbol{r}_i$ denotes the position of site i, and $d_0 = a_L/\sqrt{3}$, $d_1 = 0$ for the honeycomb lattice, and $d_0 = a_L/(2\sqrt{3})$, $d_1 = a_L/2$ for the honeycomb-kagome lattice. We constructed the GB and HKB by rotating a wedge with inner angle $\frac{2\pi}{3}$ about its tip as illustrated in Fig. 2. The corresponding TBM Hamiltonian is $(3N \times 3N)$-dimensional, if each wedge comprises N sites and is given by

$$\hat{\mathcal{H}}_{\mathrm{TBM}} = \begin{pmatrix} \hat{H} & \hat{V} & \hat{V}^T \\ \hat{V}^T & \hat{H} & \hat{V} \\ \hat{V} & \hat{V}^T & \hat{H} \end{pmatrix}, \tag{6}$$

where $\hat{H}$ denotes the N-dimensional TBM Hamiltonian of the wedge-shaped lattice structure, which is the same for each subdomain in Fig. 2. The $N \times N$ coupling matrix $\hat{V}$ and its transpose $\hat{V}^T$ contain the hoppings between sites of two adjacent subdomains along their common boundary. The TBM Hamiltonian can be brought to block-diagonal form by applying a unitary transformation,

$$\hat{U}^\dagger \hat{\mathcal{H}}_{\mathrm{TB}} \hat{U} = \begin{pmatrix} \hat{H}^{\mathrm{TB}(0)} & 0_N & \hat{0}_N \\ \hat{0}_N & \hat{H}^{\mathrm{TB}(1)} & \hat{0}_N \\ \hat{0}_N & \hat{0}_N & \hat{H}^{\mathrm{TB}(2)} \end{pmatrix}, \tag{7}$$

$$\hat{H}^{\mathrm{TB}(0)} = \hat{H} + \hat{V} + \hat{V}^T,$$
$$\hat{H}^{\mathrm{TB}(1)} = \hat{H} + e^{i\frac{2\pi}{3}}\hat{V} + e^{i\frac{4\pi}{3}}\hat{V}^T,$$
$$\hat{H}^{\mathrm{TB}(2)} = \hat{H} + e^{i\frac{4\pi}{3}}\hat{V} + e^{i\frac{2\pi}{3}}\hat{V}^T,$$

with

$$\hat{U} = \frac{1}{\sqrt{3}}\begin{pmatrix} \mathbb{1}_N & e^{i\frac{4\pi}{3}}\mathbb{1}_N & e^{i\frac{4\pi}{3}}\mathbb{1}_N \\ \mathbb{1}_N & \mathbb{1}_N & e^{i\frac{2\pi}{3}}\mathbb{1}_N \\ \mathbb{1}_N & e^{i\frac{2\pi}{3}}\mathbb{1}_N & \mathbb{1}_N \end{pmatrix}, \tag{8}$$

where $\mathbb{1}_N$ denotes the N-dimensional unit matrix. The Hamiltonians $\hat{H}^{\mathrm{TB}(l)}$, $l = 0, 1, 2$, are associated with the three irreducible C_3 subspaces defined by the transformation properties Eq. (3) under rotation by $\frac{2\pi}{3}$.

In contrast, the spinor eigenfunctions of the corresponding NB cannot be classified according to their transformation properties under rotation by $\frac{2\pi}{3}$ [16]. This is only possible for each component separately. Neutrino billiards were introduced in [61]. They are governed by the Weyl equation [62] for a noninteracting spin-1/2 particle of mass m_0, which is referred to as a Dirac equation in [61] and, generally, in the context of NBs. In the two-dimensional plane $\boldsymbol{r} = (x, y)$ it is given by

$$\hat{\boldsymbol{H}}_D\boldsymbol{\psi} = (c\hat{\boldsymbol{\sigma}}\cdot\hat{\boldsymbol{p}} + m_0c^2\hat{\sigma}_z)\boldsymbol{\psi} = E\boldsymbol{\psi},\ \boldsymbol{\psi} = \begin{pmatrix}\psi_1\\ \psi_2\end{pmatrix}, \tag{9}$$

with $\hat{\boldsymbol{p}} = -i\hbar\nabla$ the momentum of the particle. Furthermore, $\hat{\boldsymbol{H}}_D$ denotes the Dirac Hamiltonian, $\hat{\boldsymbol{\sigma}} = (\hat{\sigma}_x, \hat{\sigma}_y)$, $\hat{\sigma}_{x,y,z}$ are the Pauli matrices, and $E = \hbar ck_E = \hbar ck\sqrt{1+\beta^2}$ is the energy of the particle. Here k is the free-space wave vector, and $\beta = \frac{m_0c}{\hbar k}$ is the ratio of the rest-energy momentum and free-space momentum. In Ref. [61], only the ultrarelativistic, i.e., massless case $m_0 = 0$ was considered. The particle is confined to the billiard domain Ω by imposing the boundary condition that the normal component of the local current, which is given by the expectation value of the current operator $\hat{\boldsymbol{u}} = \boldsymbol{\nabla}_p\hat{\boldsymbol{H}}_D = c\hat{\boldsymbol{\sigma}}$, $\boldsymbol{u}(\boldsymbol{r}) = c\boldsymbol{\psi}^\dagger\hat{\boldsymbol{\sigma}}\boldsymbol{\psi}$, vanishes, yielding independently of the mass [61,79]

$$\psi_2(\phi) = i\mu e^{i\alpha(\phi)}\psi_1(\phi), \tag{10}$$

where $\alpha(\phi)$ is the angle of the outward-pointing normal vector $\boldsymbol{n}(\phi)$ at $w(r_0, \phi)$ with respect to the x axis, and $\mu = \pm 1$ determines the rotational direction of the current at the boundary. We set it to unity in the calculations presented in Ref. [16]. The nonrelativistic limit is reached when the energy is close to the rest energy, $E \simeq m_0c^2$ [80], that is, for sufficiently large $\beta \to \infty$.

Like in the nonrelativistic limit Eq. (3), the eigenstates of an NB with C_3 symmetry can be grouped into three subspaces defined by their transformation properties under a rotation by $\frac{2\pi}{3}$ [49,57–59], yielding the symmetry-projected eigenstates

$$\hat{\boldsymbol{R}}^\lambda\psi_{1,2}^{(l)}(\boldsymbol{r}) = e^{i\lambda\frac{2l\pi}{3}}\psi_{1,2}^{(l)}(\boldsymbol{r}), \quad \lambda = 0, 1, 2. \tag{11}$$

However, for a given eigen-wave-number k_m, the spinor components of the corresponding eigenfunctions behave differently under rotation by $\frac{2\pi}{3}$ [16,81]. Namely, if the first component belongs to the subspace l,

$$\hat{R}\psi_{1,m}^{(l)}(\boldsymbol{r}) = e^{il\frac{2\pi}{3}}\psi_{1,m}^{(l)}(\boldsymbol{r}), \tag{12}$$

then the Dirac equation yields for the second one

$$\hat{R}\psi_{2,m}(\boldsymbol{r}) = e^{i(l-1)\frac{2\pi}{3}}\psi_{2,m}(\boldsymbol{r}), \tag{13}$$

where $l = -1$ corresponds to $l = 2$. Similarly, employing Eq. (12) in the BC Eq. (10) and the C_3 symmetry of the boundary, that is, $e^{i\alpha(\phi-\lambda\frac{2\pi}{3})} = e^{-i\lambda\frac{2\pi}{3}}e^{i\alpha(\phi)}$, gives [16,81]

$$\hat{R}\psi_{2,m}(\phi) = ie^{i\alpha(\phi-\frac{2\pi}{3})}\psi_{1,m}^{(l)}\left(\phi - \frac{2\pi}{3}\right) = e^{i(l-1)\frac{2\pi}{3}}\psi_{2,m}(\phi),$$

implying that $\psi_{2,m}(\phi) = \psi_{2,m}^{(l-1)}(\phi)$ if $\psi_{1,m}(\phi) = \psi_{1,m}^{(l)}(\phi)$, meaning that, if the first component belongs to the subspace l, then the second one belongs to the subspace $(l-1)$. This intermingling of symmetry properties has its origin in the additional spin degree of freedom [16,81]. Nevertheless, the spinor components can be classified according to the symmetry class of, e.g., the first component, and, accordingly, their eigenvalues can be assigned to symmetry-projected subspectra. Contrary to nonrelativistic QBs, the spectral properties are well described by the GUE for all subspaces if the NB has the shape of a billiard with chaotic dynamics and no mirror symmetries.

In [16] we computed the eigenvalues of the QBs and NBs for each symmetry class separately by employing boundary integral equations resulting from Green's theorem [61,79,82,83]. The eigenvalues of the GB and HKB were obtained by diagonalizing each block of the TBM Hamiltonian Eq. (7) separately. Furthermore, we computed with COMSOL MULTIPHYSICS the symmetry-projected resonance frequencies and electric-field distributions of the DB. For the DB, GB, HKB, and QB, the spectral properties of the singlets exhibit GOE statistics, those of the doublets GUE statistics [44,49,50,57–59,84–86], whereas those of the NB follow GUE for all symmetry classes. If the spectrum of a QB with C_3 symmetry is not separated according to the three subspaces, then its fluctuation properties are described by a composite ensemble, named GOE+2GUE in the following, whose matrices are block-diagonal with one GOE block and two GUE blocks of the same dimension. For the corresponding NB, the composite ensemble consists of three GUE blocks and is denoted by 3GUE. In Ref. [16], we computed the symmetry-projected eigenstates of massive NBs as described above. For too small masses, the eigenvalues corresponding to doublet partners are not degenerate, implying that we do only find agreement of the spectral properties of the NB with those of the DB, GB, and HKB around the DPs for sufficiently large mass [79], even though these exhibit a selective excitation of the two sets of valley states [87–91].

III. THE DIRAC BILLIARD

We performed experiments at superconducting conditions. The construction of the DB is explained in the caption of Fig. 1. The basic ideas are the same as in [1,8]. The cavity consists of a top plate and a basin of 3 mm depth corresponding to a cutoff frequency $f^{\rm cut} = 50$ GHz, which contains 1033 metallic cylinders. We chose $r_0 = 30a_L/\sqrt{3} \simeq 208$ mm in Eq. (1) with $a_L = 12$ mm denoting the lattice constant. The cylinder radius equals $a_L/6$. The sidewall passes through voids, implying Dirichlet BCs at these sites for the corresponding GB. The resonance frequencies were obtained from reflection and transmission spectra. For their measurement we used a Keysight N5227A Vector Network Analyzer (VNA), which sends a rf signal into the resonator at antenna a and couples it out at the same or another antenna b and records the relative phases ϕ_{ba} and the ratios of the microwave power, $\frac{P_{{\rm out},b}}{P_{{\rm in},a}} = |S_{ba}(f)|^2$, yielding the complex scattering matrix element $S_{ba} = |S_{ba}|e^{i\phi_{ba}}$ [92–94]. Nine groups of antenna ports consisting of three each, which were positioned such that the C_3 symmetry is preserved, were distributed over the whole billiard area to minimize the possibility that a resonance is missing. This happens when the electric field strength is vanishing at the position of an antenna. The antennas penetrated through holes in the lid into the cavity by about 0.2 mm. The upper part of Fig. 3 shows a measured transmission spectrum. Propagating modes are observed above the BE at $f \simeq 13.89$ GHz.

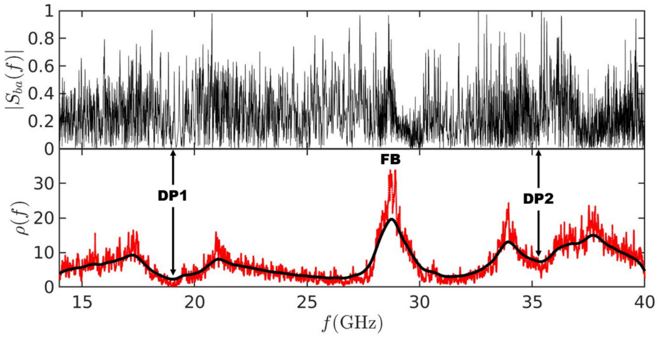

FIG. 3. Upper part: A measured transmission spectrum. The lowest band of propagating modes starts at 13.89 GHz. Lower part: DOS (red) and smoothed DOS (black). The positions of the lower and upper Dirac point (DP1 and DP2) and the FB are indicated.

The positions of the resonances yield the resonance frequencies. Degeneracies of doublet partners generally are slightly lifted due to experimental imperfection. Consequently, finding them can be cumbersome or even impossible, because corresponding resonances overlap. To identify them and to classify them into singlets and doublets, we employed a measurement method introduced in [50] and illustrated in Fig. 4. When changing the relative phase between the two ingoing signals, the position and shape of the singlets is basically not changed, whereas those of the doublets change considerably, the reason being that they are (nearly) degenerate (see Fig. 5). Thus a superposition of the associated wave functions (electric-field strength) is excited, whose phases differ [16]. This feature has been used to identify all resonance frequencies in the region of the lower BE and below the DP using the measurements with no phase shifters and with phase shifters. In total 153 measurements were performed for the nine antenna groups, 36 with no power divider and phase shifter, 9 with a power divider, and for 6 different relative phases $\Delta\phi$ with two types of phase shifters, namely for frequencies $f \in [13, 18]$ GHz with a PE8252 and for $f \in [18, 26.5]$ GHz with a P1507D; see Table I. Thereby, we were able to identify all resonance frequencies in the region of the lower BE and below the DP1. Even though the quality factor

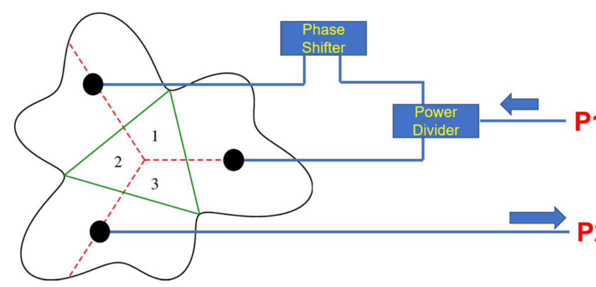

FIG. 4. Billiards with C_3 symmetry can be divided into three fundamental domains that are mapped onto each other under rotation by $\frac{2\pi}{3}$. A possible subdivision is indicated by the red dashed lines. For the measurements with phase shifters, microwaves are fed into the resonator at port P1 of the VNA and split into two signals of equal power and phase by a power divider (GF-T2-20400 with amplitude balance $\lesssim$0.4 dB and phase balance $\lesssim 5^\circ$) before they are coupled into the resonator via two antennas attached to two ports from one of the nine groups. Their relative phase $\Delta\phi$ is changed by a phase shifter (PE8253 for DC-18.6 GHz and P1507D for 18–26.5 GHz). The microwave power is received through the third antenna port at port P2 of the VNA. This process is irreversible. The shortest connected PO (green lines) has a length of $\tilde{l}_s = 11.336 r_0/3$.

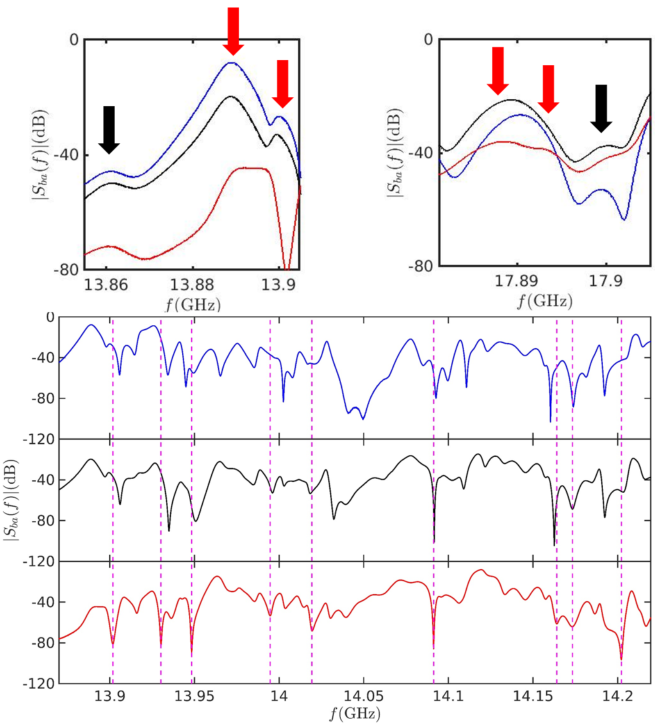

FIG. 5. Transmission spectra measured with the setup shown in Fig. 4 for relative phases $\Delta\phi = 0^\circ$ (red), $\Delta\phi = 120^\circ$ (black), and $\Delta\phi = 240^\circ$ (blue). The vertical dashed lines are plotted as guidelines to improve the visibility of the changes of the spectra with $\Delta\phi$. The insets to the left and right display the $\Delta\phi$ dependence in zooms into frequency regions comprising one singlet (black arrow) and doublet partners (red arrows).

of the resonator was $Q > 10^4$, we could not find all resonance frequencies in other regions.

In the lower part of Fig. 3 we show the density of states (DOS) $\rho(f)$ and the smoothed DOS (black curve). We observe two DPs, denoted by DP1 and DP2, van Hove singularities (VHSs) framing them, and a FB. Their frequency values are listed in Table II. Around the DP2, the DOS is distorted by an adjacent band [16]. At the FB the resonance frequencies are macroscopically degenerate in a perfect honeycomb-kagome lattice, whereas in the DB degeneracies are slightly lifted due to experimental imperfection and the spreading of the wave-function components located on the sites of the lattice. We indeed had to take into account couplings and wave-function overlaps [95] for up to third-nearest neighbors in the GB sublattice in the TBM for the HKB to get agreement with the numerical and experimental DOS [1,15,16]. In the upper part of Fig. 6, we compare the integrated spectral densities $N(f)$ obtained from the experimental and computed resonance frequencies. In total, 1912 resonance frequencies were identified in that frequency range. The curves start to differ above the lower VHS, which indicates that there not all resonance frequencies were obtained. Note that at the VHSs, the resonance frequencies are nearly degenerate [4]. Similarly, the spectral densities $\rho(f)$, shown in the lower part of Fig. 6, agree well except at the VHSs.

The frequency values of the two DPs, denoted by DP1 and DP2, VHSs framing them, and the FB are listed in Table II.

TABLE I. Measurements were performed for four different setups, for different frequency regions with or without power divider and phase shifter and different antenna combinations, as detailed in the table.

Frequency (GHz)	Power Div.	Phase Div.	#ΔΦ× antenna comb.
13–50	no	no	1 × 36
13–40	yes	no	1 × 9
18–26.5	yes	yes(PE8252)	6 × 9
13–18.6	yes	yes(P1507D)	6 × 9

IV. SPECTRAL FLUCTUATIONS

The spectral properties were analyzed below the FB in three frequency ranges, namely around the BEs, the VHSs, and in the Dirac region [1,8]. These regions are clearly distinguishable in the DOS shown in Fig. 6. We considered 189 levels for each symmetry class starting from the lower BE. Due to the presence of edge states, which lead to the peak observed in the DOS above the DP in Fig. 6 and yield nonuniversal contributions to the spectral properties [1], we only considered levels below the DP1, where each subspectrum

TABLE II. Frequencies of the lower (−) and upper (+) van Hove singularities (VHSs), around the Dirac points (DPs) (1) and (2), the centers of the band gaps (BGs), and the flat band (FB) observed in Fig. 3.

f^-_{VHS1}	f_{DP1}	f^+_{VHS1}	BG/FB
17.20 GHz	19.05 GHz	21.12 GHz	∼28.72GHz
f^-_{VHS2}	f_{DP2}	f^+_{VHS2}	BG
∼33.84 GHz	∼35.42 GHz	∼37.52 GHz	∼42.78 GHz

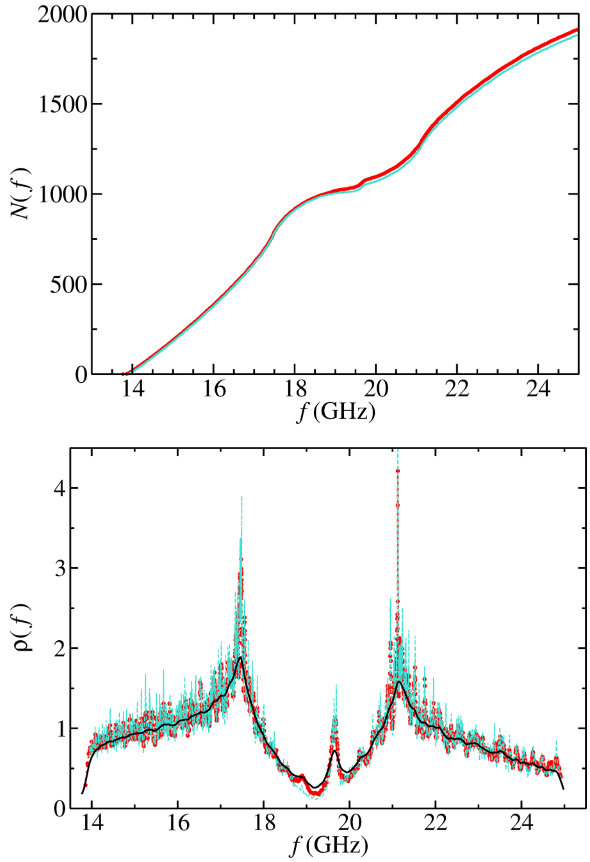

FIG. 6. Top: Integrated spectral density obtained from the experiment (red) and with COMSOL computed (turquoise) eigenfrequencies. Bottom: Same as the left part for the DOS. The black line shows the smoothed experimental DOS.

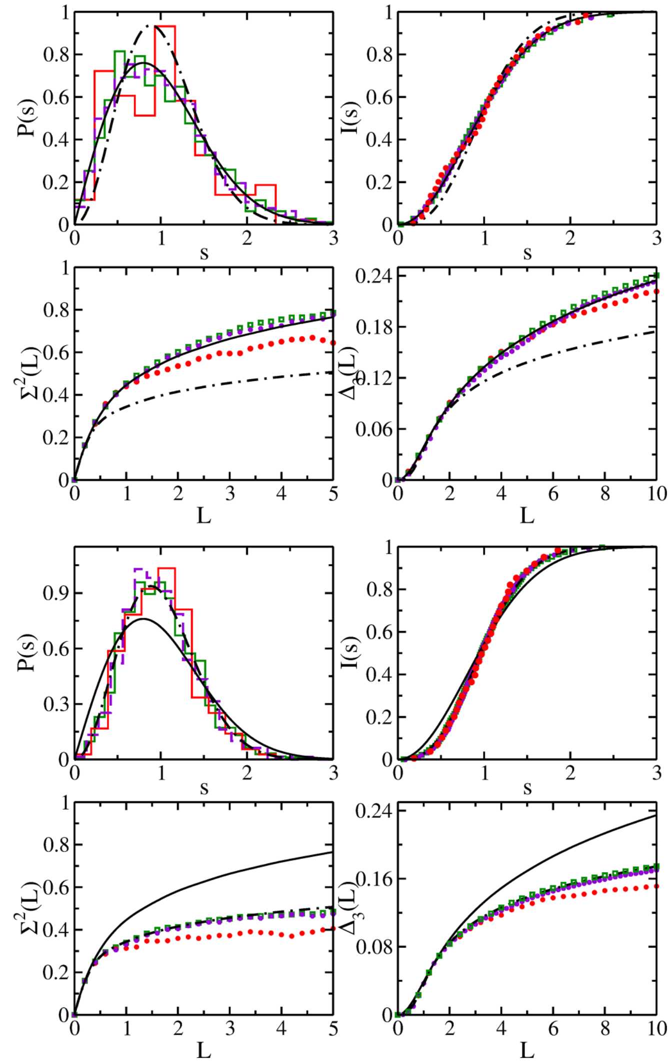

FIG. 7. Nearest-neighbor spacing distribution $P(s)$, cumulative nearest-neighbor spacing distribution $I(s)$, number variance $\Sigma^2(L)$, and Dyson-Mehta statistics $\Delta_3(L)$ for the singlets (top) and doublets (bottom) at the lower BE for the DB (red histograms and dots) and GB (green histograms and squares), and the QB (violet dashed-line histograms and stars). The solid and dashed-dotted black lines show the curves for GOE and GUE statistics, respectively.

comprises 26 levels. To unfold the resonance frequencies f_i to average spacing unity, we ordered them by size and determined the number of eigenfrequencies $N(f)$ below f. Then we replaced f_i by the smooth part of $N(f)$, $\epsilon_i = N^{\rm smooth}(f_i)$, which we determined by fitting a second-order polynomial to $N(f_i)$ [1,16]. We analyzed the spectral properties in terms of the nearest-neighbor spacing distribution $P(s)$, the integrated nearest-neighbor spacing distribution $I(s)$, the number variance $\Sigma^2(L)$ of $N(f+L) - N(f)$ in an interval of length L, and the rigidity of a spectrum of length L, $\Delta_3(L)$ [96,97]. In Fig. 7 we show the spectral properties of the singlets (top) and doublets (bottom) at the lower BE for the DB (red histograms and dots) and GB (green histograms and squares), and for the QB (violet histograms and stars). They follow the GOE curves (black solid lines) for the singlets and the GUE curves (dashed-dotted black lines) for the doublets in all cases. In Fig. 8 are plotted the spectral properties of the singlets (top) and doublets (bottom) at the DP1 for the DB (red histograms and dots) and GB (green histograms and squares), and for the NB for mass $m_0 = 0$ (maroon histograms and triangles up), $m_0 = 20$ (turquoise histograms and triangles down), and $m_0 = 100$ (orange histograms and crosses). For the DB and the GB, we find the same behavior as around the lower BE, whereas for the NB with $m_0 = 0$ the spectral properties agree with GUE for the singlets and doublets, and they are between GUE and GOE for the singlets for $m_0 = 20$. For $m_0 = 100$, the spectral properties agree well with those of the corresponding QB, that is, there the nonrelativistic limit is reached. Deviations may be attributed to the small number of levels and to the presence of short periodic orbits [16]. The shortest connected one is shown in Fig. 4. We, in addition, considered the distribution $P(r)$ and the cumulative distribution $I(r)$ of the ratios [98,99] $r_i = \frac{\epsilon_{i+1}-\epsilon_i}{\epsilon_i-\epsilon_{i-1}}$, which are dimensionless so that unfolding is not needed [8,15]. The results for all resonance frequencies below the FB are shown in the left part of Fig. 9, those of the singlets (red) and doublets (green) at the lower BE in the right part. The former are compared to those of random matrices from the GOE+2GUE. In all, the spectral properties agree well with those obtained from the COMSOL MULTIPHYSICS computations in [16] and with random-matrix

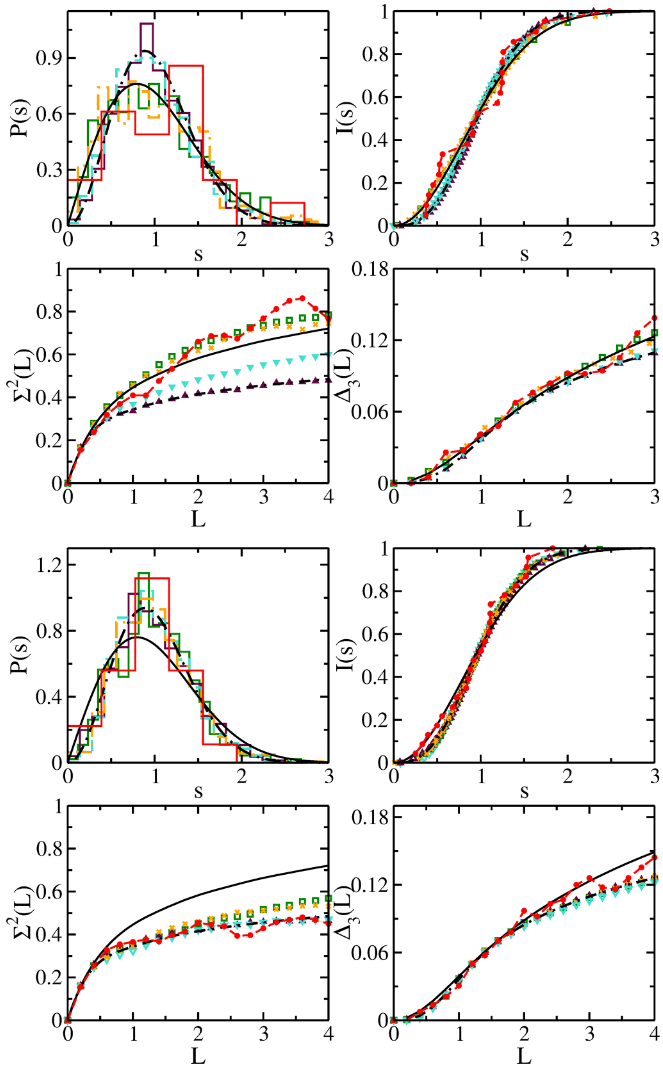

FIG. 8. Nearest-neighbor spacing distribution $P(s)$, cumulative nearest-neighbor spacing distribution $I(s)$, number variance $\Sigma^2(L)$, and Dyson-Mehta statistics $\Delta_3(L)$ for the singlets (top) and doublets (bottom) at the DP for the DB (red histograms and dots) and GB (green histograms and squares), and the NB for mass $m_0 = 0$ (maroon histogram and triangles up), $m_0 = 20$ (turquoise histograms and triangles down), and $m_0 = 100$ (orange histograms and crosses). The solid and dashed-dotted black lines show the curves for GOE and GUE statistics, respectively.

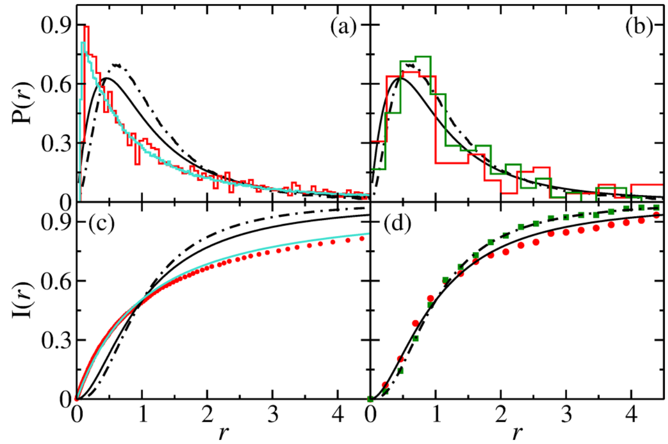

FIG. 9. Ratio distributions (upper panel) and cumulative ratio distributions (lower panels). (a), (c) All eigenfrequencies (red histogram and dots) below the FB. (b), (d) Singlets (green histogram and squares) and doublets (red histogram and dots) around the lower BE. The results are compared to those for GOE (solid black lines), GUE (dashed-dotted black lines), and GOE+2GUE (turquoise).

theory (RMT) predictions for nonrelativistic QBs with C_3 symmetry.

V. S-MATRIX FLUCTUATIONS

We also investigated the fluctuation properties of the S matrix associated with the measurement process and compared them to RMT predictions for quantum-chaotic scattering systems derived from the scattering matrix approach [100], which was developed in the context of compound nuclear reactions and extended to microwave resonators in [72],

$$S_{ba}(f) = \delta_{ba} - 2\pi i[\hat{W}^\dagger (f\mathbb{1} - \hat{H}^{\rm eff})^{-1}\hat{W}]_{ba}. \quad (14)$$

Here, $\hat{H}^{\rm eff} = \hat{H} - i\pi\hat{W}\hat{W}^\dagger$, with $\hat{H}$ modeling the universal spectral properties of the DB. Since we did not separate the resonance spectra by symmetry, we chose $\hat{H}$ random matrices from the composite ensemble GOE+2GUE and from the 3GUE for comparison. The matrix elements of $\hat{W}$ are real, Gaussian-distributed with $W_{a\mu}$ and $W_{b\mu}$ describing the coupling of the antenna channels to the resonator modes. Furthermore, we chose Λ equal fictitious channels to account for the Ohmic losses in the walls of the resonator [93,94]. Direct transmission between the antennas was negligible, so that the frequency-averaged S-matrix was diagonal, implying that $\sum_{\mu=1}^{N} W_{e\mu}W_{e'\mu} = N v_e^2 \delta_{ee'}$ [101]. The parameters v_e^2 denote the average strength of the coupling of the resonances to channels e. For $e = a, b$ they correspond to the average size of the electric field at the position of the antennas a and b and they yield the transmission coefficients $T_e = 1 - |\langle S_{ee}\rangle|^2$, which are experimentally accessible [94]. Actually, v_e and $\tau_{\rm abs} = \Lambda T_c$ are the input parameters of the RMT model Eq. (14) where they are assumed to be frequency-independent. This is fulfilled because we analyzed data in windows of size $\leqslant$1 GHz [94]. We considered three parts of the DB, defined by the location of the antennas a and b, namely an inner region (groups 1,2) around the center of the billiard domain, a middle region (groups 3,4,5,6), and an outer region (groups 7,8,9); see Fig. 1. In Fig. 10, distributions of the rescaled transmission amplitudes are shown around the lower (a) and upper (b) BE, and around the lower (c) and upper (d) VHS. At the BEs the distributions do not depend on the positions of the antennas and are well described by the RMT model Eq. (14) both for the GOE+2GUE (green) and the 3GUE (turquoise) case, which, actually, are barely distinguishable. There the wave functions are similar to those of the corresponding QB [16]. For the lower VHS and for the FB, shown in Fig. 11, we only find good agreement with the RMT results for the inner group. Otherwise we do not find any agreement around the VHSs and FB. Instead, these distributions are well described by the S-matrix model Eq. (14) when using power-law banded

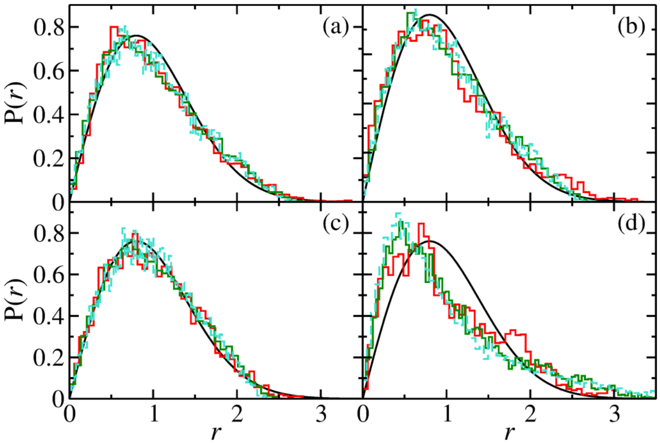

FIG. 10. Distributions of the transmission amplitudes $r = |S_{12}|/\langle|S_{12}|\rangle$ (red histogram) in (a) the region around the lower band edge $f \in [15, 16]$ GHz for antennas 4, 5, and 6; (b) same as (a) for the upper band edge $f \in [23, 24]$ GHz; (c) around the lower VHS $f \in [17.3, 17.6]$ GHz for antennas 1 and 2; and (d) the same as (c), but for the upper VHS $f \in [21, 21.3]$ GHz. They are compared to distributions obtained from the RMT model Eq. (14) with $\hat{H}$ from the GOE+2GUE (green histograms) and 3GUE (turquoise histograms). Best fit is found for $T_1 = 0.57$, $T_2 = 0.55$ and (a) $\tau_{\rm abs} = 1.0$, (b) $\tau_{\rm abs} = 0.8$, and for $T_1 = 0.67$, $T_2 = 0.69$ and $\tau_{\rm abs} = 1.0$ (c). In (d) we use corresponding PLBMs with $\alpha = 0.3$ and otherwise the same values as in (c). The black solid lines exhibit the bivariate Gaussian expected in the Ericson regime.

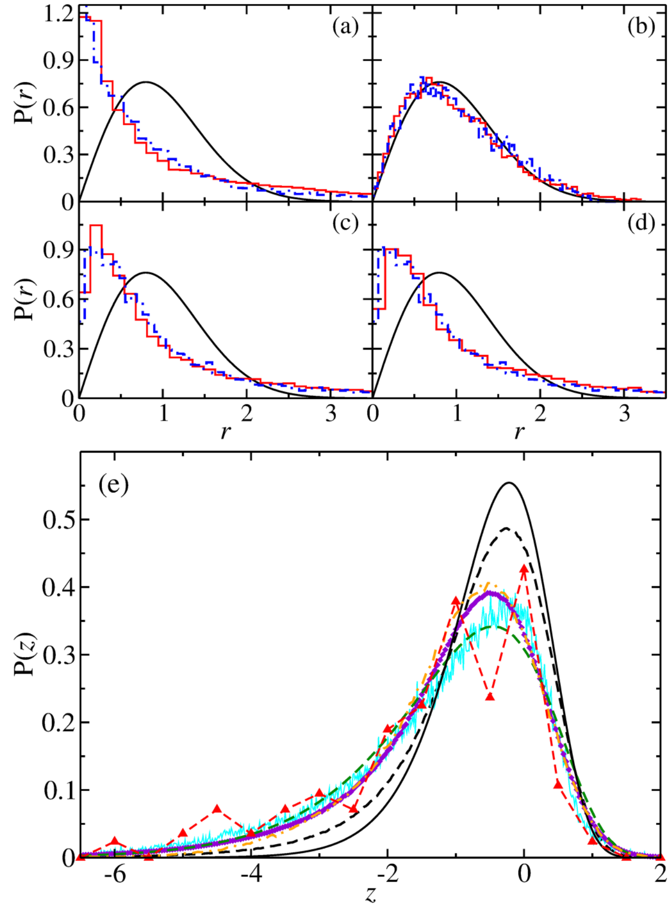

FIG. 11. (a)–(c) Distributions of the transmission amplitudes $r = |S_{12}|/\langle|S_{12}|\rangle$ (red histograms) measured in the FB $f \in [28, 29]$ GHz with all antennas (a); with antennas 1 and 2 (b); with antennas 3, 4, 5, and 6 (c); and with antennas 7, 8, and 9 (d). They are compared to the RMT model Eq. (14) with the PLBMs (blue histograms) generated from random matrices from the GOE+2GUE for $T_1 = 0.67$, $T_2 = 0.69$, $\tau_{\rm abs} = 1.0$ and $\alpha = 1.0$ (a), $\alpha = 0.1$ (b), and $\alpha = 0.7$ in (c) and (d). The black solid lines exhibit the bivariate Gaussian expected in the Ericson regime. (e) Strength distribution in the Dirac region $f \in [18.4, 19.1]$ (red triangles) obtained from antenna groups 7, 8, and 9, and from the computed wave functions of the GB in the same outer region (cyan line). They are compared to the analytical results for GOE (green dashed line), 3GUE (black solid line), GOE+2GUE (black dashed line), and to RMT simulations for PLBMs with $\alpha \simeq 0.7$–0.8 for 3GUE (orange dashed-dotted line) and GOE+2GUE (violet diamonds).

random matrices (PLBM) [102], obtained by multiplying the off-diagonal elements H_{ij} of $\hat{H}$ by a factor $|i-j|^{-\alpha}$. This ensemble interpolates between localized ($\alpha \gtrsim 1$) and extended ($\alpha = 0$) states. This is demonstrated in Fig. 10(d) and in Figs. 11(a)–11(d). Thus these deviations may be attributed to localization of the electric-field intensity in parts of the DB.

In Fig. 12 we show typical intensity distributions of the electric field strength of the DB and of the wave functions of the corresponding GB in Fig. 13. Examples are shown for the region below the flat band for singlets (first column) and corresponding doublets (second and third columns), from top to bottom, around the lower BE (first row), around the lower VHS (second row), around the DP (third row), around the upper VHS (fourth row), and for the DB also in the region of FB (fifth row). The wave functions of the doublet partners are superpositions of the corresponding symmetry-projected states with $l = 1, 2$, and thus their intensity distributions exhibit different patterns. Around the BE, the intensity distributions are mostly spread over the whole billiard domain, some are localized around shortest periodic orbits, e.g., the connected one is shown in Fig. 4, whereas around the VHS we observe, especially for the upper VHS, a strong localization around periodic orbits in the bulges of the billiard. Accordingly, we observe deviations from RMT predictions in the corresponding S-matrix amplitude distributions for the middle and outer antenna groups, whereas good agreement is found when using power-law banded random matrices in Eq. (3). Note that the amplitudes of the resonances depend on the electric-field strength at the position of the measuring antennas, and their distributions are obtained from averaging over all symmetry classes.

At the DP the resonances are well isolated. Therefore, in that region we can obtain information on the properties of the wave-function components in terms of the strength distribution [73]. Namely, for sufficiently isolated resonances, the S-matrix has the form

$$S_{ab} = \delta_{ab} - i\frac{\sqrt{\Gamma_{\mu a}\Gamma_{\mu b}}}{f - f_\mu + \frac{i}{2}\Gamma_\mu} \tag{15}$$

close to the μth resonance frequency f_μ, with Γ_μ denoting the total width of the corresponding resonance [103].

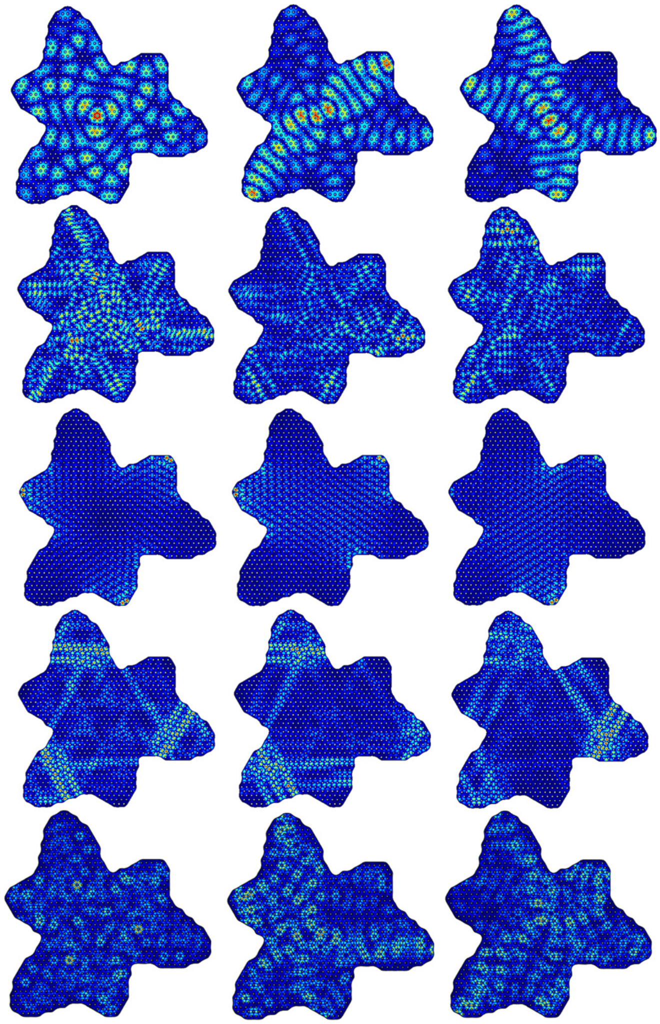

FIG. 12. Computed distributions of the electric-field intensity of the DB of the singlets (first column) and doublets (second and third columns) corresponding to state number n with resonance frequency f_n in the region below the flat band for, from top to bottom, the lower BE, the lower VHS, the lower DP, and the upper VHS. The first row shows, from left to right, examples for $n = 94$, $f_n = 14,46$ GHz, $n = 104$, $f_n = 14.52$ GHz, $n = 105$, $f_n = 14.53$ GHz; the second row for $n = 716$, $f_n = 17.224$ GHz, $n = 717$, $f_n = 17.232$ GHz, $n = 718$, $f_n = 17.235$ GHz; the third row for $n = 1007$, $f_n = 19.03$ GHz, $n = 1008$, $f_n = 19.073$ GHz, $n = 1009$, $f_n = 19.073$ GHz; the fourth row for $n = 1252$, $f_n = 21.066$ GHz, $n = 1253$, $f_n = 21.072$ GHz, $n = 1254$, $f_n = 21.072$ GHz; and the fifth row for $n = 2560$, $f_n = 28.7503$ GHz, $n = 2561$, $f_n = 28.7506$ GHz, $n = 2562$, $f_n = 28.7507$ GHz.

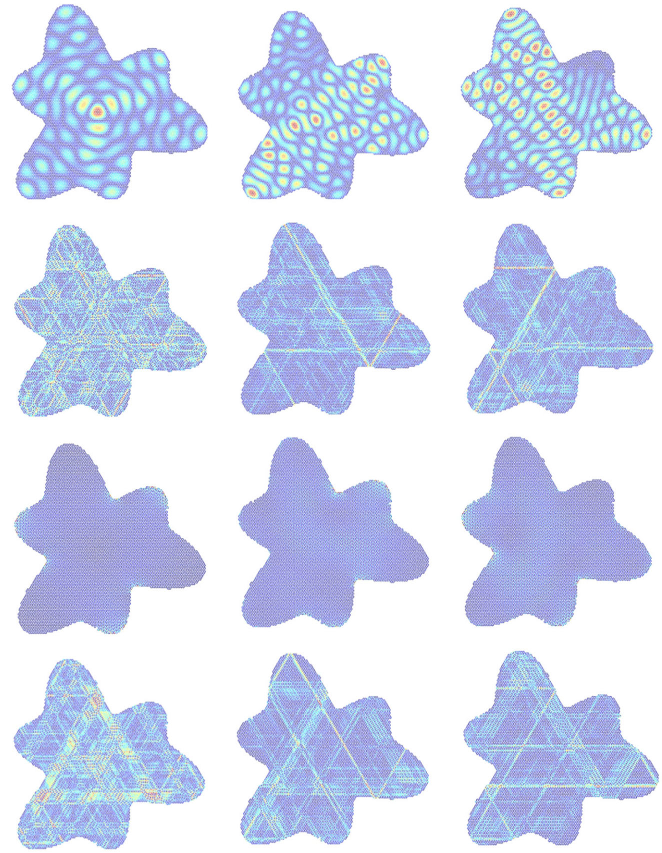

FIG. 13. Computed distributions of the wave-function intensity of the singlets (first column) and doublets (second and third columns) of the GB corresponding to state number n for, from top to bottom, the lower BE, the lower VHS, the lower DP1, and the upper VHS. The first row shows, from left to right, examples for $n = 94, 164, 165$, the second row for $n = 5897, 5918, 5919$, the third row for $n = 7981, 7982, 7983$, and the fourth row for $n = 10011, 10013, 10014$.

The partial widths $\Gamma_{\mu a}$ and $\Gamma_{\mu b}$ are proportional to the electric-field intensities at antennas a and b. They cannot be determined individually, however the strengths $z = \Gamma_{\mu a}\Gamma_{\mu b}$ may be obtained with high precision by fitting this expression to the resonances [73]. The strength distribution corresponds to the distribution of the products of the squared moduli of two wave-function components in the DB, or of two eigenvector components for the associated RMT model [74,104]. For 3GUE it coincides with that of GUE, $P^{\rm GUE}(z) = 2K_0(2\sqrt{z})$. That of GOE+2GUE is given by $P^{\rm GOE+2GUE}(z) = \frac{1}{3}[P^{\rm GOE}(z) + 2P^{\rm GUE}(z)]$, where $P^{\rm GOE}(z) = K_0(\sqrt{z})/(\pi\sqrt{z})$. Here, $K_0(z)$ denotes the modified Bessel function of order zero. In Fig. 11(e) we compare these analytical expressions to the distributions obtained for the DB in the Dirac region (red triangles). However, like for the FB, we find only agreement with the RMT distributions, when using the corresponding PLBM $\alpha \simeq 0.7$–0.8, where that for GOE+2GUE (violet diamonds) is better than that for 3GUE (orange dashed-dotted lines).

VI. CONCLUSIONS

We performed experiments with a superconducting DB, whose shape has a C_3 symmetry. To identify the resonance frequencies and to separate them into the three symmetry classes, we successfully employed a procedure that was originally developed for hollow microwave billiards [50], thereby demonstrating that it is applicable even to complex structures like the DB. We confirm results that were obtained in Ref. [16] from numerical computations, namely, find good agreement of the spectral properties with those of the QB, GB, and HKB of corresponding shape, and with those of massive relativistic NBs only beyond a certain mass. We also investigated the properties of the wave functions below the DP1, where the DOS is low, in terms of the strength distribution. We find good agreement with the corresponding distributions of random matrices from GOE+2GUE when using PLBMs, corroborating that the wave functions are localized [3]. Yet, the spectral properties of the associated resonance frequencies agree well with those of typical quantum systems with a C_3 symmetry and a chaotic classical dynamics. Furthermore, we investigated the fluctuation properties of the measured S matrix in the regions around the BEs, the VHSs, and the FB, which are not accessible numerically. In the nonrelativistic regime, we find good agreement with those of the RMT model Eq. (14) for GOE+2GUE, whereas for the other regions we took account of the localization observed in parts of the DB by using PLBMs. Around the VHSs, the ratio distributions agree well with those of random matrices from the GOE+2GUE. From these observations we may conclude that even in regions where the wave functions are localized in parts of the DB, the spectral properties comply with those of typical quantum systems whose corresponding classical dynamics is chaotic [8].

ACKNOWLEDGMENTS

This work was supported by the NSF of China under Grants No. 11775100, No. 12247101, and No. 11961131009. W.Z. acknowledges financial support from the China Scholarship Council (No. CSC-202106180044). B.D. and W.Z. acknowledge financial support from the Institute for Basic Science in Korea through Project No. IBS-R024-D1.

[1] B. Dietz, T. Klaus, M. Miski-Oglu, and A. Richter, Spectral properties of superconducting microwave photonic crystals modeling Dirac billiards, Phys. Rev. B **91**, 035411 (2015).

[2] S. Bittner, B. Dietz, M. Miski-Oglu, P. Oria Iriarte, A. Richter, and F. Schäfer, Observation of a Dirac point in microwave experiments with a photonic crystal modeling graphene, Phys. Rev. B **82**, 014301 (2010).

[3] S. Bittner, B. Dietz, M. Miski-Oglu, and A. Richter, Extremal transmission through a microwave photonic crystal and the observation of edge states in a rectangular Dirac billiard, Phys. Rev. B **85**, 064301 (2012).

[4] B. Dietz, F. Iachello, M. Miski-Oglu, N. Pietralla, A. Richter, L. von Smekal, and J. Wambach, Lifshitz and excited-state quantum phase transitions in microwave Dirac billiards, Phys. Rev. B **88**, 104101 (2013).

[5] F. Iachello, B. Dietz, M. Miski-Oglu, and A. Richter, Algebraic theory of crystal vibrations: Singularities and zeros in vibrations of one- and two-dimensional lattices, Phys. Rev. B **91**, 214307 (2015).

[6] B. Dietz and A. Richter, Quantum and wave dynamical chaos in superconducting microwave billiards, Chaos **25**, 097601 (2015).

[7] B. Dietz, T. Klaus, M. Miski-Oglu, A. Richter, M. Bischoff, L. von Smekal, and J. Wambach, Fullerene C_{60} Simulated with a Superconducting Microwave Resonator and Test of the Atiyah-Singer Index Theorem, Phys. Rev. Lett. **115**, 026801 (2015).

[8] B. Dietz, T. Klaus, M. Miski-Oglu, A. Richter, M. Wunderle, and C. Bouazza, Spectral Properties of Dirac Billiards at the van Hove Singularities, Phys. Rev. Lett. **116**, 023901 (2016).

[9] B. Dietz and A. Richter, From graphene to fullerene: Experiments with microwave photonic crystals, Phys. Scr. **94**, 014002 (2019).

[10] U. Kuhl, S. Barkhofen, T. Tudorovskiy, H.-J. Stöckmann, T. Hossain, L. de Forges de Parny, and F. Mortessagne, Dirac point and edge states in a microwave realization of tight-binding graphene-like structures, Phys. Rev. B **82**, 094308 (2010).

[11] T. Jacqmin, I. Carusotto, I. Sagnes, M. Abbarchi, D. D. Solnyshkov, G. Malpuech, E. Galopin, A. Lemaître, J. Bloch, and A. Amo, Direct Observation of Dirac Cones and a Flatband in a Honeycomb Lattice for Polaritons, Phys. Rev. Lett. **112**, 116402 (2014).

[12] Z. Lan, N. Goldman, and P. Öhberg, Coexistence of spin-$\frac{1}{2}$ and spin-1 Dirac-Weyl fermions in the edge-centered honeycomb lattice, Phys. Rev. B **85**, 155451 (2012).

[13] J.-L. Lu, W. Luo, X.-Y. Li, S.-Q. Yang, J.-X. Cao, X.-G. Gong, and H.-J. Xiang, Two-dimensional node-line semimetals in a honeycomb-kagome lattice, Chin. Phys. Lett. **34**, 057302 (2017).

[14] H. Zhong, Y. Zhang, Y. Zhu, D. Zhang, C. Li, Y. Zhang, F. Li, M. R. Belić, and M. Xiao, Transport properties in the photonic super-honeycomb lattice–a hybrid fermionic and bosonic system, Ann. Phys. **529**, 1600258 (2017).

[15] W. Maimaiti, B. Dietz, and A. Andreanov, Microwave photonic crystals as an experimental realization of a combined honeycomb-kagome lattice, Phys. Rev. B **102**, 214301 (2020).

[16] W. Zhang and B. Dietz, Microwave photonic crystals, graphene, and honeycomb-kagome billiards with threefold symmetry: Comparison with nonrelativistic and relativistic quantum billiards, Phys. Rev. B **104**, 064310 (2021).

[17] K. S. Novoselov, A. K. Geim, S. V. Morozov, D. Jiang, Y. Zhang, S. V. Dubonos, I. V. Grigorieva, and A. A. Firsov, Electric field effect in atomically thin carbon films, Science **306**, 666 (2004).

[18] C. W. J. Beenakker, Colloquium: Andreev reflection and klein tunneling in graphene, Rev. Mod. Phys. **80**, 1337 (2008).

[19] A. H. Castro Neto, F. Guinea, N. M. R. Peres, K. S. Novoselov, and A. K. Geim, The electronic properties of graphene, Rev. Mod. Phys. **81**, 109 (2009).

[20] D. P. DiVincenzo and E. J. Mele, Self-consistent effective-mass theory for intralayer screening in graphite intercalation compounds, Phys. Rev. B **29**, 1685 (1984).

[21] A. Geim and K. Novoselov, The rise of graphene, Nat. Mater. **6**, 183 (2007).

[22] P. Avouris, Z. Chen, and V. Perebeinos, Carbon-based electronics, Nat. Nanotechnol. **2**, 605 (2007).

[23] F. Miao, S. Wijeratne, Y. Zhang, U. C. Coskun, W. Bao, and C. N. Lau, Phase-coherent transport in graphene quantum billiards, Science **317**, 1530 (2007).

[24] L. A. Ponomarenko, F. Schedin, M. I. Katsnelson, R. Yang, E. W. Hill, K. S. Novoselov, and A. K. Geim, Chaotic Dirac billiard in graphene quantum dots, Science **320**, 356 (2008).

[25] X. Zhang and Z. Liu, Extremal Transmission and Beating Effect of Acoustic Waves in Two-Dimensional Sonic Crystals, Phys. Rev. Lett. **101**, 264303 (2008).

[26] D. Abergel, V. Apalkov, J. Berashevich, K. Ziegler, and T. Chakraborty, Properties of graphene: A theoretical perspective, Adv. Phys. **59**, 261 (2010).

[27] S. R. Zandbergen and M. J. A. de Dood, Experimental Observation of Strong Edge Effects on the Pseudodiffusive Transport of Light in Photonic Graphene, Phys. Rev. Lett. **104**, 043903 (2010).

[28] M. Polini, F. Guinea, M. Lewenstein, H. C. Manoharan, and V. Pellegrini, Artificial graphene as a tunable dirac material, Nat. Nanotechnol. **8**, 625 (2013).

[29] P. V. Parimi, W. T. Lu, P. Vodo, J. Sokoloff, J. S. Derov, and S. Sridhar, Negative Refraction and Left-Handed Electromagnetism in Microwave Photonic Crystals, Phys. Rev. Lett. **92**, 127401 (2004).

[30] S. Joannopoulos, J. D. Johnson, R. Meade, and J. Winn, *Photonic Crystals. Molding the Flow of Light* (Princeton University Press, Princeton, NJ, 2008).

[31] A. Singha, M. Gibertini, B. Karmakar, S. Yuan, M. Polini, G. Vignale, M. I. Katsnelson, A. Pinczuk, L. N. Pfeiffer, K. W. West, and V. Pellegrini, Two-dimensional mott-hubbard electrons in an artificial honeycomb lattice, Science **332**, 1176 (2011).

[32] L. Nádvorník, M. Orlita, N. A. Goncharuk, L. Smrčka, V. Novák, V. Jurka, K. Hruška, Z. Výborný, Z. R. Wasilewski, M. Potemski, and K. Výborný, From laterally modulated two-dimensional electron gas towards artificial graphene, New J. Phys. **14**, 053002 (2012).

[33] K. K. Gomes, W. Mar, W. Ko, F. Guinea, and H. C. Manoharan, Designer Dirac fermions and topological phases in molecular graphene, Nature (London) **483**, 306 (2012).

[34] L. Tarruell, D. Greif, T. Uehlinger, G. Jotzu, and T. Esslinger, Creating, moving and merging Dirac points with a Fermi gas in a tunable honeycomb lattice, Nature **483**, 302 (2012).

[35] T. Uehlinger, G. Jotzu, M. Messer, D. Greif, W. Hofstetter, U. Bissbort, and T. Esslinger, Artificial Graphene with Tunable Interactions, Phys. Rev. Lett. **111**, 185307 (2013).

[36] M. C. Rechtsman, Y. Plotnik, J. M. Zeuner, D. Song, Z. Chen, A. Szameit, and M. Segev, Topological Creation and Destruction of Edge States in Photonic Graphene, Phys. Rev. Lett. **111**, 103901 (2013).

[37] M. C. Rechtsman, J. M. Zeuner, A. Tünnermann, S. Nolte, M. Segev, and A. Szameit, Strain-induced pseudomagnetic field and photonic Landau levels in dielectric structures, Nat. Photon. **7**, 153 (2013).

[38] A. B. Khanikaev, S. H. Mousavi, W.-K. Tse, M. Kargarian, A. H. MacDonald, and G. Shvets, Photonic topological insulators, Nat. Mater. **12**, 233 (2013).

[39] X. Wang, H. T. Jiang, C. Yan, F. S. Deng, Y. Sun, Y. H. Li, Y. L. Shi, and H. Chen, Transmission properties near Dirac-like point in two-dimensional dielectric photonic crystals, Europhys. Lett. **108**, 14002 (2014).

[40] Z. Shi, G. Lin, T.-H. Xiao, H.-L. Guo, and Z.-Y. Li, All-optical modulation of a graphene-cladded silicon photonic crystal cavity, Photonics **2**, 1513 (2015).

[41] M. Bellec, U. Kuhl, G. Montambaux, and F. Mortessagne, Topological Transition of Dirac Points in a Microwave Experiment, Phys. Rev. Lett. **110**, 033902 (2013).

[42] M. Bellec, U. Kuhl, G. Montambaux, and F. Mortessagne, Tight-binding couplings in microwave artificial graphene, Phys. Rev. B **88**, 115437 (2013).

[43] M. Bellec, U. Kuhl, G. Montambaux, and F. Mortessagne, Manipulation of edge states in microwave artificial graphene, New J. Phys. **16**, 113023 (2014).

[44] C. Dembowski, H.-D. Gräf, A. Heine, H. Rehfeld, A. Richter, and C. Schmit, Gaussian unitary ensemble statistics in a time-reversal invariant microwave triangular billiard, Phys. Rev. E **62**, R4516 (2000).

[45] M. V. Berry and M. Tabor, Calculating the bound spectrum by path summation in actionangle variables, J. Phys. A **10**, 371 (1977).

[46] M. Berry, *Structural Stability in Physics* (Pergamon, Berlin, 1979).

[47] G. Casati, F. Valz-Gris, and I. Guarnieri, On the connection between quantization of nonintegrable systems and statistical theory of spectra, Lett. Nuovo Cimento **28**, 279 (1980).

[48] O. Bohigas, M. J. Giannoni, and C. Schmit, Characterization of Chaotic Quantum Spectra and Universality of Level Fluctuation Laws, Phys. Rev. Lett. **52**, 1 (1984).

[49] F. Leyvraz, C. Schmit, and T. H. Seligman, Anomalous spectral statistics in a symmetrical billiard, J. Phys. A **29**, L575 (1996).

[50] C. Dembowski, B. Dietz, H.-D. Gräf, A. Heine, F. Leyvraz, M. Miski-Oglu, A. Richter, and T. H. Seligman, Phase Shift Experiments Identifying Kramers Doublets in a Chaotic Superconducting Microwave Billiard of Threefold Symmetry, Phys. Rev. Lett. **90**, 014102 (2003).

[51] O. Knill, On nonconvex caustics of convex billiards, Elemente Math. **53**, 89 (1998).

[52] B. Gutkin, Dynamical "breaking" of time reversal symmetry, J. Phys. A **40**, F761 (2007).

[53] G. Veble, T. Prosen, and M. Robnik, Expanded boundary integral method and chaotic time-reversal doublets in quantum billiards, New J. Phys. **9**, 15 (2007).

[54] B. Dietz, T. Guhr, B. Gutkin, M. Miski-Oglu, and A. Richter, Spectral properties and dynamical tunneling in constant-width billiards, Phys. Rev. E **90**, 022903 (2014).

[55] L. G. C. Rego, A. Gusso, and M. G. E. da Luz, Anomalous quantum chaotic behaviour in suspended electromechanical nanostructures, J. Phys. A **38**, L639 (2005).

[56] A. Gusso, M. G. E. da Luz, and L. G. C. Rego, Quantum chaos in nanoelectromechanical systems, Phys. Rev. B **73**, 035436 (2006).

[57] J. M. Robbins, Discrete symmetries in periodic-orbit theory, Phys. Rev. A **40**, 2128 (1989).

[58] J. P. Keating and J. M. Robbins, Discrete symmetries and spectral statistics, J. Phys. A **30**, L177 (1997).

[59] C. H. Joyner, S. Müller, and M. Sieber, Semiclassical approach to discrete symmetries in quantum chaos, J. Phys. A **45**, 205102 (2012).

[60] P. R. Wallace, The band theory of graphite, Phys. Rev. **71**, 622 (1947).

[61] M. V. Berry and R. J. Mondragon, Neutrino billiards: Time-reversal symmetry-breaking without magnetic fields, Proc. R. Soc. London A **412**, 53 (1987).

[62] H. Weyl, Elektron und Gravitation. I, Z. Phys. **56**, 330 (1929).
[63] P. Yu, Z.-Y. Li, H.-Y. Xu, L. Huang, B. Dietz, C. Grebogi, and Y.-C. Lai, Gaussian orthogonal ensemble statistics in graphene billiards with the shape of classically integrable billiards, Phys. Rev. E **94**, 062214 (2016).
[64] P. Yu, W. Zhang, B. Dietz, and L. Huang, Quantum signatures of chaos in relativistic quantum billiards with shapes of circle- and ellipse-sectors*, J. Phys. A **55**, 224015 (2022).
[65] P. G. Silvestrov and K. B. Efetov, Quantum Dots in Graphene, Phys. Rev. Lett. **98**, 016802 (2007).
[66] F. Libisch, C. Stampfer, and J. Burgdörfer, Graphene quantum dots: Beyond a Dirac billiard, Phys. Rev. B **79**, 115423 (2009).
[67] J. Wurm, A. Rycerz, İ. Adagideli, M. Wimmer, K. Richter, and H. U. Baranger, Symmetry Classes in Graphene Quantum Dots: Universal Spectral Statistics, Weak Localization, and Conductance Fluctuations, Phys. Rev. Lett. **102**, 056806 (2009).
[68] L. Huang, Y.-C. Lai, and C. Grebogi, Relativistic quantum level-spacing statistics in chaotic graphene billiards, Phys. Rev. E **81**, 055203(R) (2010).
[69] J. Wurm, K. Richter, and İ. Adagideli, Edge effects in graphene nanostructures: From multiple reflection expansion to density of states, Phys. Rev. B **84**, 075468 (2011).
[70] A. Rycerz, Random matrices and quantum chaos in weakly disordered graphene nanoflakes, Phys. Rev. B **85**, 245424 (2012).
[71] A. Rycerz, Strain-induced transitions to quantum chaos and effective time-reversal symmetry breaking in triangular graphene nanoflakes, Phys. Rev. B **87**, 195431 (2013).
[72] S. Albeverio, F. Haake, P. Kurasov, M. Kuś, and P. Šeba, S-matrix, resonances, and wave functions for transport through billiards with leads, J. Math. Phys. **37**, 4888 (1996).
[73] C. Dembowski, B. Dietz, T. Friedrich, H.-D. Gräf, H. L. Harney, A. Heine, M. Miski-Oglu, and A. Richter, Distribution of resonance strengths in microwave billiards of mixed and chaotic dynamics, Phys. Rev. E **71**, 046202 (2005).
[74] B. Dietz, T. Guhr, H. L. Harney, and A. Richter, Strength Distributions and Symmetry Breaking in Coupled Microwave Billiards, Phys. Rev. Lett. **96**, 254101 (2006).
[75] H.-J. Stöckmann and J. Stein, “Quantum” Chaos in Billiards Studied by Microwave Absorption, Phys. Rev. Lett. **64**, 2215 (1990).
[76] S. Sridhar, Experimental Observation of Scarred Eigenfunctions of Chaotic Microwave Cavities, Phys. Rev. Lett. **67**, 785 (1991).
[77] H.-D. Gräf, H. L. Harney, H. Lengeler, C. H. Lewenkopf, C. Rangacharyulu, A. Richter, P. Schardt, and H. A. Weidenmüller, Distribution of Eigenmodes in a Superconducting Stadium Billiard with Chaotic Dynamics, Phys. Rev. Lett. **69**, 1296 (1992).
[78] F. Haake, S. Gnutzmann, and M. Kuś, *Quantum Signatures of Chaos* (Springer-Verlag, Heidelberg, 2018).
[79] B. Dietz and Z.-Y. Li, Semiclassical quantization of neutrino billiards, Phys. Rev. E **102**, 042214 (2020).
[80] G. Baym, *Lectures on Quantum Mechanics* (CRC, Boca Raton, FL, 2018).
[81] B. Dietz, Relativistic quantum billiards with threefold rotational symmetry: Exact, symmetry-projected solutions for the equilateral neutrino billiard, Acta Phys. Pol. A **140**, 473 (2021).
[82] A. Bäcker, Numerical Aspects of Eigenvalue and Eigenfunction Computations for Chaotic Quantum Systems, in *The Mathematical Aspects of Quantum Maps*, edited by M. D. Esposti and S. Graffi (Springer, Berlin, 2003), pp. 91–144.
[83] B. Dietz, Unidirectionality and Husimi functions in constant-width neutrino billiards, J. Phys. A **55**, 474003 (2022).
[84] P. Braun, F. Leyvraz, and T. H. Seligman, Correlations between spectra with different symmetries: Any chance to be observed? New J. Phys. **13**, 063027 (2011).
[85] R. Schäfer, M. Barth, F. Leyvraz, M. Müller, T. H. Seligman, and H.-J. Stöckmann, Transition from Gaussian-orthogonal to Gaussian-unitary ensemble in a microwave billiard with threefold symmetry, Phys. Rev. E **66**, 016202 (2002).
[86] T. H. Seligman and H. A. Weidenmüller, Semi-classical periodic-orbit theory for chaotic Hamiltonians with discrete symmetries, J. Phys. A **27**, 7915 (1994).
[87] J. Lu, C. Qiu, S. Xu, Y. Ye, M. Ke, and Z. Liu, Dirac cones in two-dimensional artificial crystals for classical waves, Phys. Rev. B **89**, 134302 (2014).
[88] J. Lu, C. Qiu, M. Ke, and Z. Liu, Valley Vortex States in Sonic Crystals, Phys. Rev. Lett. **116**, 093901 (2016).
[89] J. Lu, C. Qiu, L. Ye, X. Fan, M. Ke, F. Zhang, and Z. Liu, Observation of topological valley transport of sound in sonic crystals, Nat. Phys. **13**, 369 (2017).
[90] L. Ye, C. Qiu, J. Lu, X. Wen, Y. Shen, M. Ke, F. Zhang, and Z. Liu, Observation of acoustic valley vortex states and valley-chirality locked beam splitting, Phys. Rev. B **95**, 174106 (2017).
[91] B.-Z. Xia, T.-T. Liu, G.-L. Huang, H.-Q. Dai, J.-R. Jiao, X.-G. Zang, D.-J. Yu, S.-J. Zheng, and J. Liu, Topological phononic insulator with robust pseudospin-dependent transport, Phys. Rev. B **96**, 094106 (2017).
[92] B. Dietz, T. Friedrich, H. L. Harney, M. Miski-Oglu, A. Richter, F. Schäfer, and H. A. Weidenmüller, Chaotic scattering in the regime of weakly overlapping resonances, Phys. Rev. E **78**, 055204(R) (2008).
[93] B. Dietz, T. Friedrich, H. L. Harney, M. Miski-Oglu, A. Richter, F. Schäfer, J. Verbaarschot, and H. A. Weidenmüller, Induced Violation of Time-Reversal Invariance in the Regime of Weakly Overlapping Resonances, Phys. Rev. Lett. **103**, 064101 (2009).
[94] B. Dietz, T. Friedrich, H. L. Harney, M. Miski-Oglu, A. Richter, F. Schäfer, and H. A. Weidenmüller, Quantum chaotic scattering in microwave resonators, Phys. Rev. E **81**, 036205 (2010).
[95] S. Reich, J. Maultzsch, C. Thomsen, and P. Ordejón, Tight-binding description of graphene, Phys. Rev. B **66**, 035412 (2002).
[96] O. Bohigas and M. J. Giannoni, Level density fluctuations and random matrix theory, Ann. Phys. **89**, 393 (1975).
[97] M. L. Mehta, *Random Matrices* (Elsevier, Amsterdam, 2004).
[98] V. Oganesyan and D. A. Huse, Localization of interacting fermions at high temperature, Phys. Rev. B **75**, 155111 (2007).
[99] Y. Y. Atas, E. Bogomolny, O. Giraud, and G. Roux, Distribution of the Ratio of Consecutive Level Spacings in Random Matrix Ensembles, Phys. Rev. Lett. **110**, 084101 (2013).

[100] C. Mahaux and H. A. Weidenmüller, *Shell Model Approach to Nuclear Reactions* (North Holland, Amsterdam, 1969).

[101] J. Verbaarschot, H. Weidenmüller, and M. Zirnbauer, Grassmann integration in stochastic quantum physics: The case of compound-nucleus scattering, Phys. Rep. **129**, 367 (1985).

[102] A. D. Mirlin, Y. V. Fyodorov, F.-M. Dittes, J. Quezada, and T. H. Seligman, Transition from localized to extended eigenstates in the ensemble of power-law random banded matrices, Phys. Rev. E **54**, 3221 (1996).

[103] H. Alt, H. D. Gräf, H. L. Harney, R. Hofferbert, H. Lengeler, A. Richter, P. Schardt, and H. A. Weidenmüller, Gaussian Orthogonal Ensemble Statistics in a Microwave Stadium Billiard with Chaotic Dynamics: Porter-Thomas Distribution and Algebraic Decay of Time Correlations, Phys. Rev. Lett. **74**, 62 (1995).

[104] T. Guhr, A. Müller-Groeling, and H. A. Weidenmüller, Random-matrix theories in quantum physics: Common concepts, Phys. Rep. **299**, 189 (1998).